Noninvasive technology of photostimulation of lymphatic clearance of red blood cells from the mouse brain after intraventricular hemorrhage.

Dongyu Li
Huazhong University of Science and Technology
Shaojun Liu
Huazhong University of Science and Technology
Tingting Yu
Huazhong University of Science and Technology
Zhang Liu
Huazhong University of Science and Technology
Silin Sun
Huazhong University of Science and Technology
Denis Bragin
Lovelace Biomedical Research Institute
Alexander Shirokov
Institute of Biochemistry and Physiology of Plants and Microorganisms, Russian Academy of Sciences
Nikita Navolokin
Saratov Medical State University https://orcid.org/0000-0001-7876-9758
Olga Bragina
Lovelace Biomedical Research Institute
Juergen Kurths
Potsdam Institute for Climate Impact Research https://orcid.org/0000-0002-5926-4276
Ivan Fedosov
Saratov State University
Oxana Semyachkina-Glushkovskaya
Saratov State University
Dan Zhu (dawnzh@mail.hust.edu.cn)
Huazhong University of Science and Technology https://orcid.org/0000-0002-3640-4758

Article

Keywords: intraventricular hemorrhage (IVH), brain injury, hematoma

Posted Date: May 17th, 2021

DOI: https://doi.org/10.21203/rs.3.rs-87930/v1

Abstract

Intraventricular hemorrhage (IVH) is the most fatal form of brain injury in adults and infants. However, therapy of IVH is very limited, and new strategies are needed to reduce hematoma expansion. For the first time, in our experiments on mice with IVH, we clearly demonstrate that transcranial low-level infra-red photostimulation (PS) accelerates the red blood cells (RBCs) evacuation from the ventricles that is associated with reducing the mortality in 1.57 times, improving emotional status and recovery of intracranial pressure. We revealed the mechanisms of PS-modulation of lymphatic contractility and tone of the lymphatic vessels underlying the lymphatic clearing functions. Our findings strongly suggest that PS-mediated stimulation of lymphatic clearance of RBCs can be a novel non-invasive, bedside, readily applicable, and commercially viable technology for the treatment of IVH.

Introduction

Brain hemorrhage in adults and premature infants has the highest morbidity and mortality worldwide [1-3]. Intraventricular hemorrhage (IVH) is bleeding into the brain's ventricular system, where the cerebrospinal fluid (CSF) is produced and circulates through towards the subarachnoid space. About 30% of IVHs primarily result from trauma, and 70% are secondary, i.e., originate from spontaneous intracranial hemorrhage (ICH) [4-6]. Both adult and neonatal patients with IVH have mortality from 50% to 80% and are twice as likely to have poor outcomes [2,7-9]. The IVH occurs in 45% of premature infants and 46-50% of mature babies [10-12]. About 45–85% of premature infants with moderate-to-severe IVH develop significant cognitive deficits, and approximately 75% of these infants need special education in school [13].

Blood in the ventricular system contributes to morbidity in a variety of ways. Pressure from the leaked blood damages brain cells, disabling the proper function of the injured area. Besides, red blood cell (RBC) lysis after IVH results in the release of blood breakdown products (hemoglobin, iron, and bilirubin). Such products have been implicated in the post-hemorrhagic hydrocephalus' pathophysiology and an increase in intracerebral pressure (ICP) because of impairment of CSF circulation and the brain drainage system [14, 15]. Therefore, the conventional therapy of IVH, including surgery and fibrinolysis in combination with extraventricular drainage, aimed at the blood evacuation from the ventricles, both for reducing ICP induced by mass effects of blood clots on the ventricular walls and the secondary damage caused by blood cell lysis [6, 16, 17]. However, the existing therapy of IVH has dramatically impacted the natural history of the disease and new strategies are needed to reduce hematoma expansion and improve the drainage system of the brain [6, 16, 17].

Photostimulation (PS) can be an innovative technology targeted to the therapy of IVH. The transcranial PS is considered the non-pharmacological and non-invasive therapy of stroke [18-20] and traumatic brain injuries [21-23]. There is strong evidence that PS can regulate the relaxation and permeability of the lymphatic vessels (LVs), activate the movement of immune cells in the lymph, and have effectiveness in the management of lymphedema [24-26]. Our preliminary work clearly demonstrated that the near-

infrared PS (1267 nm) stimulates clearance of tracers from the brain via modulation of lymphatic tone and contraction [24, 25]. We also showed that PS (1267 nm) effectively stimulates lymphatic clearance of beta-amyloid from the brain [27].

In this work, we investigate whether PS (1267 nm) can enhance RBCs evacuation from the ventricles to improve the outcome after IVH. We clearly demonstrate the lymphatic clearance of RBCs from the brain in the post-hemorrhagic period. We found that PS has therapeutic effects on IVH in mice reducing mortality 1.57 times, improving emotional status, accelerating the RBCs evacuation from the ventricles, and increasing the ICP recovery. We investigated the possible mechanisms underlying PS-mediated the lymphatic contractility and tone of LVs. Our findings open new horizons in non-invasive therapy of IVH via PS stimulation of the lymphatic drainage and clearing functions that can be a novel bedside, readily applicable and commercially viable technologies for effective routine treatment of IVH.

Results

Lymphatic clearance of RBCs from mouse and human brain

RBCs can be cleared from the brain [28, 29] and subarachnoid space [30] into dcLNs. We, therefore, examined the lymphatic pathway of RBCs removing from the mouse brain into dcLNs after IVH. The confocal colocalization analysis of dcLNs stained for two classical markers of the lymphatic (Lyve-1 and Prox-1) and the blood endothelium cells (CD-31) revealed the presence of RBCs in dcLNs of mice with IVH (Fig. 1b). The RBCs were observed inside LVs of dcLNs 3 hours after IVH. There were no RBCs in LVs of dcLNs in intact mice (Fig. 1a).

Theoretically, following IVH, RBCs can be evacuated to the subarachnoid space via CSF movement and penetrate MLVs, which drain them to dcLNs [28,29] (Fig. S1). Therefore, we analyzed the RBCs presence in subarachnoid space and meninges, stained with Lyve1/Prox1 and CD31. The confocal colocalization analysis demonstrated that RBCs were observed in both subarachnoid space and meningeal lymphatic vessels (MLVs) of IVH mice but not in intact mice (Fig. 2a-2l). In addition, we analyzed the human meninges stained with Lyve1 (LEC marker), CD31 (the blood endothelium marker), and Glycophorin A (GPA, RBCs marker). The human data indicated that RBCs were also presented in MLVs after IVH (Fig. 2m-2p).

These results suggest the lymphatic pathway of RBCs clearance from mouse and human brain, which is consistent with the oldest and latest data of lymphatic efflux of RBCs from the brain [28, 29] and the meninges [30].

PS stimulates lymphatic clearance of RBCs and macromolecules from the brain

It is well known that irradiation wavelength range starting from 1100 nm and longer begins to be absorbed by water [31] and can cause significant heating effects on the water content of biological objects. As demonstrated [32, 33], brain functions are so sensitive to the changes in temperatures that an

increase of 0.5° C can cause significant alterations in the cellular processes. 1° C and above can cause profound effects on neural network functioning. Therefore, we measured the temperature on the skull (the scalp removed) and the top of the cortex for five laser doses of 3-6-9-18-27 J/cm^2.

The temperature on the external skull surface was increased by 0.11-0.14-0.19-0.70-1.83 °C after PS 3-6-9-18-27 J/cm^2 (Table S1). The application of these small PS doses was not accompanied by any changes in the cortex surface temperature (Table S1). Thus, the laser doses of 3-6-9-18-27 J/cm^2 did not induce any significant increase in the brain tissues temperature and cannot affect the brain morphology and functionality.

To find the effective PS dose for lymphatic clearance stimulation we studied the clearance of gold nanorods (GNRs) from the right lateral ventricle during 60 min in healthy mice (Fig. S2, Table S2). Using in vivo optical coherence tomography (OCT), we found that the rate of GNRs accumulation in dcLNs was minimal in the control group (no PS) and was not changed after PS 3 J/cm^2 and 6 J/cm^2 (Table S2). However, the rate of GNRs accumulation in dcLN was 1.4-fold ($p<0.001$) higher after PS 9 J/cm^2 (Fig. 3c and S2). There was no further increase in the intensity of GNRs accumulation in dcLNs using higher PS doses 18 J/cm^2 (Fig. S3, Table S2).

To confirm these findings, we performed a quantitative analysis of GNRs level in dcLNs using atomic absorption spectroscopy (Table S3). The *ex vivo* results confirmed the OCT data and showed that the level of GNRs in dcLNs was not changed after PS 3 J/cm^2 and 6 J/cm^2 and was 3.17-fold ($p<0.001$) higher after PS 9 J/cm^2; 2.95-fold ($p<0.001$) higher after 18 J/cm^2; 3.27-fold ($p<0.001$) higher after 27 J/cm^2.

Additionally, we used fluorescent microscopy for *in vivo* imaging of Evans Blue dye (EBD) clearance from the right ventricle before and after PS (Fig. S3). Indeed, the intensity of EBD fluorescence in dcLNs during 60 min was not changed after PS 3 J/cm^2 and 6 J/cm^2 and was 2.54-fold ($p<0.001$) higher after PS 9 J/cm^2; 2.66-fold ($p<0.001$) higher after 18 J/cm^2 ; 2.62-fold ($p<0.001$) higher after 27 J/cm^2 (Table S4 and Fig. 3a-3b).

Thus, our results on healthy mice demonstrate that PS doses 3 J/cm^2 and 6 J/cm^2 were not sufficient for PS-stimulation of lymphatic clearance of GRNs and EBD. In contrast, PS doses 9-18-27 J/cm^2 caused similar effects on GNRs and EBD accumulation in dcLNs. However, PS doses 18 J/cm^2 and 27 J/cm^2 were accompanied by an increase in the skull temperature that can induce the heating effects on red blood cells [34]. Therefore, PS 9 J/cm^2 on the skull (3 J/cm^2 on the brain surface, the measuring method see Fig. S4) has been selected as an optimal for further experiments.

Using established protocol for PS on healthy mice, we studied PS 9 J/cm^2 effects on the RBCs clearance from the brain in mice after IVH. The results presented in Fig. 3d-3j clearly demonstrate that the number

of RBCs in dcLNs was significantly higher in the group IVH+PS vs. the IVH group without PS ((5.7±1.4)×10^5 per mm^3 vs. (1.7±0.7)×10^5 per mm^3, p<0.001). There were no RBCs in the sham group.

PS reduces the intracranial pressure (ICP), the mortality rate and improves the emotional status after IVH

In the next step, we studied the therapeutic effects of PS after IVH in mice. Figure 4a clearly demonstrates that IVH is accompanied by a dramatic rise in ICP that was significantly improved by PS. So, the blood injection into the right ventricle immediately caused an increase in ICP (75.5 ±12.5 mm Hg vs.10.2 ± 2.1 mm Hg, p<0.01 for the IVH group and 74.2 ± 11.4 mm Hg vs.10.2 ± 2.1 mm Hg, p<0.01 for the IVH+PS group). Afterward, ICP gradually decreased but remained to be high by the end of 60 min monitoring. The PS significantly reduced the time of ICP recovery. Indeed, the recovery of ICP in the IVH+PS group was faster than in the IVH group (29.0 ± 3.1 mm Hg vs. 19.6 ± 3.2 mm Hg at 60 min of monitoring, respectively, p<0.05).

Since the recovery after IVH requires long-term therapy, we studied the effects of the PS-9 J/cm^2 course (the total PS dose was 63 J/cm^2) performed every day over one week on the mortality and emotional disorders in mice after IVH. The mortality of mice was 36.7% (11 of 30) in the IVH group. No animals died in the sham groups (n=30). PS course increased the survival of mice. So, the mortality in the IVH+PS group was 23.3% (7 of 30), i.e., 1.57-fold lesser than in the IVH group (Fig. 4b).

The tail suspension and forced swim tests were used for evaluating the emotional abnormality after IVH. The time of immobility in the tail suspension and forced swim tests were longer in the IVH than in the sham group (n=10 in each group, p<0.001; Fig. 4c and 4d). PS course was accompanied by a significant decrease of immobility time in both tail suspension and forced swim tests compared to the IVH group (p<0.05, n=10 in each group). PS did not affect the performance of both tests in the sham group.

Thus, these results suggest that PS contributes to a faster recovery of ICP after IVH. PS-course causes a 1.57-fold decrease in mortality and improves the emotional status of mice with IVH.

The mechanisms of PS effects on the lymphatic vessels

Recent work has shown that basal MLVs have the valves as the peripheral collecting lymph vessels and are hotspots for the clearance of CSF macromolecules [35]. We found that the diameter of basal MLVs was higher in the IVH+PS group vs. IVH without PS group (31.0±12.80 μm vs. 25.75±15.71 μm, p<0.01) and the sham group (31.0±12.80 μm vs. 25.80±14.26 μm, p<0.01, Fig. 5a-f).

The mechanism by which PS affects the lymphatics has not been adequately explored. There is evidence that it might be via PS-mediated stimulation of nitric oxide (NO) production [36-39]. NO is a vasodilator that modulates the lymphatic vessel contractility and subsequent lymph flow via multiple points in the Ca^{2+}-contraction pathway [40,41].

Considering these facts, we hypothesized that PS-mediated lymphatic removal of RBCs from the mouse brain might be due to PS-stimulation of NO production in the lymphatic endothelium and PS-increase in

the lymphatic vessels contractility. The MLVs express all of the molecular hallmarks of lymphatic proteins typical for the peripheral lymphatic vessels [42]. There is not real-time technologies for monitoring of MLVs functions because it is extremely thin and small vessels. We, therefore, used the mesenteric lymphangion for monitoring of PS effects on the lymphatic contractility and NO production as a model of study of lymphatic functions. Our OCT data revealed that PS 3 J/cm^2 (PS dose was similar to those on the brain surface) significantly increased the lymphangion contraction (Fig. 5g and 5h, movie S1 and S2). In *in vitro* experiments on the isolated lymphatic cells (LECs) from the mesenteric tissue, we showed a significant increase in the 24 h accumulation of NO_2^- in the cell culture medium after PS 3 J/cm^2 compared with the accumulation of NO_2^- produced by LECs without PS (Fig. 5i). Thus, these findings suggest PS stimulates NO generation in LECs associated with an increase in contraction of the lymphatic vessels.

Discussion

In this study, we reveal that PS modulates the RBCs clearance from the right lateral ventricle of mice with IVH accompanied by 1.57 times mortality reduction, emotional status improvement, and intracranial pressure recovery.

In *ex vivo* experiments using mouse and human brain samples, we clearly demonstrated the lymphatic clearance of RBCs from the brain after IVH. These results provide strong support for the old theory of RBCs evacuation from the brain via lymphatic efflux [28,29,43]. Our data are also consistent with the newest discovery of the meningeal lymphatic pathway of clearance of RCBs after subarachnoid hemorrhage [30]. Thus, augmentation of the lymphatic evacuation of RBCs from the brain might be a promising tool for the therapy of IVH.

Here we investigated the effects of infra-red PS (1267 nm) on the lymphatic removal of RBCs from the brain and the outcome after IVH. The infra-red light of 800-1100 nm widely used for the PS therapy of brain diseases [18-23]**.** However, the infra-red PS has a significant limitation, such as limited penetration into the brain due to light scattering and heating effect [44]. The light wavelength of 1300 nm has less scattering and can penetrate deeper into the brain [45]. Therefore, we selected optimal PS (1267 nm) dose for the experiments studying the light transmission and the changes in the temperature on the skull and the surface of the brain after PS 3-6-9-18-27 J/cm^2. Our data clearly demonstrate that PS 9 J/cm^2 vs. other PS doses was most effective for stimulating lymphatic clearance of GNRs and EBD without heating effect that determined our choice of PS 9 J/cm^2 as the optimal dose for further investigations.

In *in vivo* experiments, we uncover that PS 9 J/cm^2 accelerates the RBCs evacuation from the ventricles. The seven-day PS 9 J/cm^2 course has therapeutic effects on mice with IVH reducing mortality 1.57 times, improving the emotional status and increasing the ICP recovery. Our results align with other animal and human data suggesting a greater clinical significance of transcranial near-infrared laser phototherapy of stroke and brain trauma [18-23].

To study mechanisms of therapeutic effects of PS, we investigated PS influences on the diameter of basal MLVs as well as on the NO production in LEC and the lymphatic contractility as the main factors underlying lymphatic drainage and clearing functions. Our findings demonstrate that PS dilated MLVs and increased NO production in LEC of isolated lymphatic cells are associated with an increase in the lymphangion contraction. These results suggest that PS-mediated activation of NO synthesis in LEC and the lymphatic contractility might be the possible mechanisms responsible for PS-stimulation of lymphatic clearance of RBCs and macromolecules from the brain. The described effects can be related to a PS-mediated increase in the activity of endothelial nitric oxide (NO) synthase [36]. NO is a vasodilator that acts via stimulation of soluble guanylate cyclase to form cyclic-GMP (cGMP), which activates protein kinase G causing the opening of calcium-activated potassium channels and reuptake of Ca^{2+}. The decrease in the concentration of Ca^{2+} prevents myosin light-chain kinase from phosphorylating the myosin molecule, leading to relaxation of lymphatic vessels [46]. There are several other mechanisms by which NO could control the lymphatic tone and contractility: 1) the activation of an iron-regulatory factor in macrophages [47], 2) the modulation of proteins such as ribonucleotide reductase [48] and aconitase [49]; the stimulation of the ADP-ribosylation of glyceraldehyde-3-phosphate dehydrogenase [50] and protein-sulfhydryl-group nitrosylation [51]. In our previous work, we revealed that PS causes relaxation of the mesenteric lymphatic endothelium associated with an increase inpermeability of lymphatic walls and decreased expression of tight junction proteins [25]. We assume that the PS effects on the tone of MLVs facilitate drainage in fluid spaces of the brain that drains RBCs/macromolecules from the ventricles along with the subarachnoid space, where RBCs partly penetrate MLVs.

Conclusion

Our findings open new horizons in a non-invasive therapy of IVH. The PS-mediated stimulation of lymphatic clearance of RBCs can be a novel bedside, readily applicable and commercially viable technology for effective routine treatment of IVH and other types of brain bleedings. Our pilot experiments were focused on demonstrating the lymphatic clearance of RBCs and the mechanisms underlying this phenomenon that needs further detailed investigations of clinical efficiency of PS-mediated stimulation of lymphatic functions in the human brain. Due to the scattering effects of the skull, the laser penetration into the brain is very limited that is the most complication of PS. However, PS-acceleration of RBCs clearance from the brain via MLVs can be clinically significant for brain hemorrhages therapy in newborns where PS can be applied through the newborn brain's fontanelle. Note that IVH occurs in 45% of premature infants [10-12]. The PS-lymphatic therapy can also be useful for superficially located silent subarachnoid and subdural hemorrhages identified in 46-50% of mature babies [10-12].

Methods

Subjects

Autopsy specimens of human dura were obtained from the Department of Pathological Anatomy at the Saratov State University (average age 42). All obtained samples were fixed and stored in a 10% formalin

solution for prolonged periods. The human studies were performed on the control group, including 7 patients with congestive heart failure with pulmonary edema, and in the experimental group, including 8 patients who died from the primary and secondary intraventricular hemorrhages.

Male BALB/c mice (20–25 g) were used in all experiments. The animals were housed under standard laboratory conditions, with access to food and water, *ad libitum*. All procedures were performed in accordance with the “Guide for the Care and Use of Laboratory Animals”. The experimental protocols were approved by the Local Bioethics Commission of the Saratov State University (Protocol No. 7); Experimental Animal Management Ordinance of Hubei Province, P. R. China (No. 1000639903375); the Institutional Animal Care and Use Committee of the University of New Mexico, USA (#200247). The animal experiments included the following groups: 1) the intact, healthy mice; 2) the IVH group were injected the autologous blood into the right lateral ventricle; 3) sham control mice were injected an equal volume of saline; 4) sham + photostimulation (PS) group, and 5) the IVH group+PS.

Mouse intraventricular hemorrhage model

To produce the mouse IVH model, autologous blood was injected into the right lateral ventricle. Aseptic techniques were used in all surgical procedures. The disinfection with Betadine and 70% ethanol of the stereotactic apparatus and surgical tools were made prior to surgery. Throughout surgery and the experimental period, rectal temperature was monitored until mice completely recovered and displayed normal motor activity. The ketamine (100 mg/kg) and xylazine (10 mg/kg) was injected intraperitoneally for the anesthesia. The mouse was placed onto a thermal blanket and the scalp was shaved. The ophthalmic ointment to both eyes was applied. A 1 cm long midline incision of the scalp with a 10 scalpel blade was made. The Hamilton syringe (25 μl) was mounted onto the injection pump, and the needle (25 Gauge) over bregma was directed stereotaxically. Next, the needle was positioned 0.5 mm posterior and 1.06 mm lateral of the bregma to the right with the stereotactic manipulator. A small cranial burr hole was drilled through the skull using a variable speed drill with a 1 mm drill bit. The animal's tail was disinfected with 70% ethanol and the central tail artery was punctured with a sterile needle (25 Gauge), then the arterial blood was fixed with heparin sodium and collected into a capillary tube. The 10 μl of blood was quickly transferred from the capillary tube into the glass barrel of the Hamilton syringe and inserted the plunger. The needle was inserted into the right lateral ventricle to a depth of 2.5 mm below the skull surface. The arterial blood was injected at a rate of 2 μl/min. The needle was left in the ventricle for 10 min and then removed at a rate of 1 mm/min to prevent the reflux of blood. The burr hole and scalp incision were closed with bone wax (Ethicon, Somerville, NJ) and with cyanoacrylate glue (Henkel Consumer Adhesive Inc. Scottsdale, Arizona), respectively. Sham control mice were injected with an equal volume (10 μl) of saline.

Laser radiation scheme and dose calculation

A fibre Bragg grating wavelength locked high-power laser diode (LD-1267-FBG-350, Innolume, Dortmund, Germany) emitting at 1267 nm was used as a source of irradiation. The laser diode was pigtailed with a single-mode distal fiber ended by the collimation optics to provide a 5 mm beam diameter at the

specimen. The mice with shaved head were fixed in a stereotaxic frame under inhalation anesthesia (1% isoflurane at 1 L/ min N_2O/O_2 – 70/30 ratio) and irradiated in the area of the Sagittal sinus using a single laser dose (3-6-9-18-27 J/cm^2) or the PS course 63 J/cm^2 during 7 days with the sequence of 17 min – irradiation, 5 min – pause, 61 min in total). For the PS course, the mice were treated daily by PS for 7 days under inhalation anesthesia (1% isoflurane at 1 L/min N_2O/O_2 - 70:30) 3 days after the surgery procedure of blood injection into the right lateral ventricle (Fig. S1).

The transmission analysis of the 1267 nm laser irradiation passing through freshly prepared mouse scull sample revealed a scattering effect giving 1.2 times wider laser beam of 5-mm diameter. Only 35% of initial laser energy reached the top layer of the cortex (Fig. S4). The laser doses were calculated as followed:

$$D = \left[\frac{0.35 \times P}{1.44 \times S}\right] \times T \qquad (1)$$

Where D is irradiation dose; 0.35 - optical transmission and 1.44 - scattering coefficients, correspondently; S is square of the laser beam on the brain cortex (cm^2); P is a laser irradiation power on the skull surface (W); T is the time of laser irradiation. Thereby, the entire PS course comprising 17 min PS + 5 min pause + 17 min PS + 5 min pause + 17 min PS of 2.4 mW laser power intensities applied gave 9 J/cm^2 (on the skull) and 3 J/cm^2 on the brain surface daily doses for each animal, irradiated. Subsequently, the whole PS course where animals were irradiated every day for 1 week finally gave 63 J/cm^2 doses.

Measurement of the PS' thermal impact

A type A-K3 thermocouple (Ellab, Hillerød, Denmark) was used to measure skull temperature. The thermocouple was placed subcutaneously 2 mm lateral to the bregma in the irradiated zone. A burr hole was drilled under inhalation anesthesia (1% isoflurane at 1 L/min N_2O/O_2—70:30). To measure the brain surface temperature under the 1267 nm laser irradiation, the medial part of the left temporal muscle was detached from the skull bone, a small burr hole was drilled into the temporal bone, and a flexible thermocouple probe (IT-23, 0.23 mm diam, Physitemp Instruments LLC, NJ, USA) was introduced between the parietal bone and brain into the epidural space. Brain surface temperature was measured before and during the laser stimulation with 5 minutes increment using a handheld thermometer (BAT-7001H, Physitemp Instruments LLC, NJ, USA).

Immunohistochemistry (IHC) and confocal imaging

To visualize LVs, fluorescent markers were used to label specific structures using the immunohistochemical method [42]. Anti-Lyve-1 and anti-Prox-1 antibodies were used to label LVs; anti-CD-31 antibody was used to label blood vessels.

Mice were sacrificed with cervical dislocation. To obtain the meninges, the skin was removed from the head, and the muscle was stripped from the bone. After removing the mandibles and the skull rostral to maxillae, the top of the skull was removed with surgical scissors. Whole-mount meninges were fixed while still attached to the skull cap in PBS with 2% paraformaldehyde (PFA) overnight at 4 ℃. The meninges were then dissected from the skull. For analysis of dcLNs, the lymph nodes were removed and fixed in PBS with 2% PFA overnight at 4 ℃, and then fixed in 2% agarose, followed by sliced into 60 μm-thick sections using a vibratome (Leica VT1000, Germany).

The whole mounts of meninges and the sections of dcLNs were firstly washed 3 times (5 min for each) with wash solution (0.2% Triton-X-100 in PBS), secondly incubated in the blocking solution (a mixture of 2% Triton-X-100 and 5% normal goat serum in PBS) for 1 hour, followed by incubation with Alexa Fluor 488-conjugated anti-Lyve-1 antibody (1:500; FAB2125G, R&D Systems, Minneapolis, Minnesota, USA), rabbit anti-Prox-1 antibody (1:500; ab 101851, Abcam, Cambridge, United Kingdom) and mouse Alexa Fluor 647-conjugated anti-CD31 antibody (1:500; 102416 BioLegend, San Diego, USA) overnight at 4°C in PBS containing 0.2% Triton-X-100 and 0.5% normal goat serum. Next, the meninges were incubated at room temperature for 1 hour and then washed 3 times, followed by incubation with goat anti-rabbit IgG (H+L) Alexa Fluor 561 (Invitrogen, Molecular Probes, Eugene, Oregon, USA).

For visualization of human LVs in the dura mater, the protocol for IHC was used with Lyve-1 ((ab219556; Abcam, Biomedical Campus Cambridge, Cambridge, UK). Briefly, tissue samples were fixed with formaldehyde and, after routine processing, were embedded into a paraffin block. Then the samples were sectioned into 3- to 5-μm slides; afterward, they were dried at 37°C for 24 h and then rehydrated by sequential incubation in xylene (three times, 3 min each), 96% ethanol (three times, 3 min each), 80% ethanol (two times, 3 min each), and distilled water (three times, 3 min each). The IHC reaction was visualized with a REVEAL—BiotinFree Polyvalent diaminobenzidine kit (Spring Bioscience). Endogenous peroxidases were blocked by adding 0.3% hydrogen peroxide to the sections for 10 min, followed by washing of sections in phosphate-buffered saline (PBS). The antigen retrieval was conducted using a microwave oven in an ethylenediaminetetraacetic acid-buffer pH 9.0, and a nonspecific background staining was blocked in PBS containing 0.5% bovine serum albumin and 0.5% casein for 10 min, after which the sections were washed in PBS for 5 min. Further, the sections were incubated in a humid chamber with diluted anti-Lyve-1 ((ab219556; Abcam, Biomedical Campus Cambridge, Cambridge, UK 1:1000)) for 1 h at room temperature. After that, the sections were washed in PBS, incubated with secondary horseradish peroxidase-labeled goat antirabbit antibodies for 15 min, again washed in PBS, counterstained with hematoxylin for 1 min, washed again in water, dehydrated in graded alcohols (three times, 3 min each) and then in xylene (three times, 3 min each), and finally embedded into Canadian balm.

For confocal visualization of LVs in the human meninges, the protocol for IHC was used with antibodies to the lymphatic endothelial cells - Lyve1 (ab219556; Abcam, Biomedical Campus Cambridge, Cambridge, UK, 1:500) and for the blood endothelium CD31 (ab187377; Abcam, Biomedical Campus Cambridge, Cambridge, UK, 1:500) and to RBC' – anti-glycophorin A (GPA, ab33386; Abcam, Biomedical Campus

Cambridge, Cambridge, UK, 1:500)). The brain tissues were collected and free-floating sections were prepared. Pieces of the brain, measuring 2x2 cm, were fixed for 48 hours in a 4% saline solution-buffered formalin, then sections of the brain with a thickness of 40-50 microns were cut on a vibratome (Leica Microsystems GmbH, Germany). Brain sections were processed according to the standard IHC protocol with the corresponding primary and secondary antibodies. Confocal microscopy of human brain sections was performed using a Leica SP8 confocal laser scanning microscope (Leica Microsystems GmbH, Germany). The nonspecific activity was blocked by 2-hour incubation at room temperature with 10% BSA in a solution of 0.2% Triton X-100 in PBS. Solubilization of cell membranes was carried out during 1-hour incubation at room temperature in a solution of 1% Triton X-100 in PBS. Incubation with primary antibodies in a 1:500 dilution was performed overnight at 4 ° C: with rabbit antibodies to Lyve-1 (1:500; ab219556; Abcam, Biomedical Campus Cambridge, Cambridge, UK); mouse antibodies to CD31 (1:500; ab187377; Abcam, Biomedical Campus Cambridge, Cambridge, UK) and rat antibodies GPA (1:500; ab33386; Abcam, Biomedical Campus Cambridge, Cambridge, UK);. At all stages, the samples were washed 3-4 times with 5-minute incubation in a washing solution. Afterward, the corresponding secondary antibodies were applied (goat anti-rat IgG (H+L) Alexa Four 647; goat anti-mouse IgG (H+L) Alexa Four 555 and goat anti -rabbit IgG (H+L) Alexa Four 405; Invitrogen, Molecular Samples, Eugene, Oregon, USA). At the final stage, the sections were transferred to the glass and 15 µl of mounting liquid (50% glycerin in PBS with DAPI at a concentration of 2 µg/ml) was applied to the section. The preparation was covered with a cover glass and confocal microscopy was performed.

The mouse meninges and dcLN sections were imaged using a confocal microscope (LSM 710, Zeiss, Jena, Germany) with a ×20 objective (0.8 NA) or a ×60 oil immersion objective (1.46 NA). Alexa Fluor 488 and Alexa Fluor 561 were excited with excitation wavelengths of 488 nm and 561 nm, respectively. Alexa Fluor 647 and RBCs were excited with the same excitation wavelength of 647 nm. Three-dimensional imaging data were collected by obtaining images from the x, y, and z-planes. The resulting images were analyzed with Imaris software (Bitplane).

Measurement of meningeal lymphatic vessel diameter

To measure the diameter of LVs, the original program with Matlab was developed (Fig. S5).

Procedure 1

This procedure was used to extract the profile of LVs from the initial image. First, Otsu's method [52] was utilized to decide the threshold and obtain the binary image (Fig. S6-Step 1). Next, an image closing operation was used to connect the broken edges of the image. Then, two Matlab functions, "imfill" and "bwareaopen", were used to fill in the holes and remove the small connected domains of the image, respectively (Fig. S6-Step 2). Finally, the obtained image was subtracted by itself after morphological corrosion, and the profile curve wasS then determined (Fig. S6-Step 3).

procedure 2

This procedure was used to calculate the diameter distribution of lymphatic vessels. As shown in Fig. S6-Step 4, point A and point B represents any points on the outlines on both sides of the lymphatic vessel, and l_1 and l_2 are the tangent lines at point A and B, respectively. If l_1, l_2 and l_{AB} follows both $l_1 \perp l_{AB}$ and $l_2 \perp l_{AB}$, i.e.

$$k_A k_{AB} = k_B k_{AB} = -1,$$

where k_A, k_B and k_{AB} present the slope of line l_1, l_2 and l_{AB}, respectively. In this case, l_{AB} could be taken as the diameter at a certain position. However, points A and B were not always successfully found in all the images. Therefore, for every point A, point B was given by

$$\min\left(|k_A k_{AB} + 1| + |k_B k_{AB} + 1|\right)$$

Following the above rule, we could obtain a series of |AB| as the lymphatic vascular diameters at every position.

Fluorescent microscopy monitoring of EBD accumulation in dcLN

Mice were anesthetized by ketamine (100 mg/kg) and xylazine (10 mg/kg) and fixed in a stereotactic apparatus, the skull exposed, and a small burr hole was made over the right lateral (AP = 0.1 mm, ML = 0.85 mm). Afterward, 5 µL of 5% EBD (Sigma-Aldrich) was injected (0.5 ml/min) into the right later ventricle to a depth of 2.5 mm DV. 20 min later, the ventral skin of the neck was cut and dcLNs were exposed. The stereo fluorescence microscope (Axio Zoom. V16, Zeiss, Jena, Germany) working at 10× magnification was used for imaging of dcLNs during 60 min before and after PS (3-6-9-18-27 J/cm^2). After imaging, the fluorescence intensity of EBD in dcLNs (a.u.) was measured using FIJI software.

OCT monitoring of GNRs accumulation in dcLN

The GNRs coated with thiolated polyethylene glycol (0.2 µL, the average diameter, and length at 16±3 nm and 92±17 nm) were injected in the right lateral ventricle (AP: -0.5 mm; DV: 2.5 mm; ML: 1.06 mm). Afterward, OCT imaging of the dcLNs was performed during the next 1h for each mouse.

In this study, a commercial spectral domain OCT Thorlabs GANYMEDE (central wavelength 930 nm, spectral band 150 nm) was used. The LSM02 objective was used to provide a lateral resolution of about 13 microns within the depth of the field. The a-scan rate of the OCT system was set to 30 kHz. Each B-scan consists of 2048 A-scans to ensure appropriate spatial sampling.

Since lymph is optically transparent in a broad range of wavelengths, “empty” cavities exist in the resulting OCT image of the lymphatic node with a background signal-to-noise ratio inside. In order to visualize the dynamic accumulation of lymph within these cavities, suspensions of GNRs were used as a

contrast agent and the OCT signal intensity is proportional to the GNRs concentration. By tracking the OCT signal temporal intensity changes inside a node's cavity, we could confirm the clearance pathways and calculate its relative speed. The OCT recordings were performed under anesthesia with ketamine (100 mg/kg, i.p.) and xylazine (10 mg/kg, i.p.).

The GNRs content in the brain tissue and in dcLNs was evaluated by atomic absorption spectroscopy on a spectrophotometer (Thermo Scientific Inc., Waltham, Massachusetts, USA). The atomic absorption spectroscopy of GNRs was performed 20-40-60 min after the start of OCT monitoring in the brain and in the dcLNs obtained from the same mice, which were used for OCT-GNRs measurements.

Intracranial pressure monitoring

The ICP monitoring was performed as described previously [53]. For this purpose, the medial part of the left temporal muscle was detached from the skull bone, a small hole was drilled into the temporal bone, and an ICP probe (TSD280) was introduced between the bone and brain into the epidural space and fixed with dental cement. ICP was continuously recorded before, during, and 60 minutes after the IVH on a laptop computer using a micro pressure measurement system (MPMS200), preamplifier (MP150), and software (Biopac, Goleta, CA).

Tests for evaluation of emotional abnormalities

Post-hemorrhage depression is the most common emotional sequelae of brain hemorrhages, and it is independently associated with increased morbidity and mortality [54, 55]. The tail suspension and forced swim test effectively evaluate emotional abnormality in different models of intracranial hemorrhages [56, 57]. Therefore, these two tests were used for the analysis of early recovery after IVH. The protocol for the tail suspension test was described previously [58, 59]. Briefly, animals were suspended by their tails at the edge of a shelf 55 cm above a desk. Sticky tape (17 cm long) was used to fix the tail (approximately 1 cm from the tip) to the shelf. The recording of mouse mobility and immobility (lack of escape-related behavior when mice hung passively and completely motionless) was made during 360 sec. The forced swim test protocol was published in detail in Ref. [60, 61]. The cylindrical tanks (20 cm high, 22 cm in diameter) with water at 24 ± 1^{0}C (10 cm) was used for this test. Each mouse was placed individually in water. The swimming of mice was recorded for 360 sec. The immobility time (when the mouse remained floating motionless, making only small movements to keep its head above the water) was calculated during the last 4 min from the 240 s of test time [58].

Isolation of lymphatic endothelial cells (LyECs)

Freshly isolated primary LyECs were obtained from the mesentery of intact mice. Briefly, the atrium was cannulated and the vascular system perfused with normal saline solution. Mesenteric lymphatic tissue mucosa was harvested, placed on 35 mm plates containing ice-cold phosphate-buffered saline, and cut into small (1 mm) fragments. The fragments were incubated in 0.25% collagenase A (Roche Diagnostics, Basel, Switzerland) at 378C. The suspension was passed through 100 mm nylon mesh and centrifuged

at 1800 rpm for 4 min at 48C. The cell pellet was resuspended in Hank's balanced salt solution. The LyECs were isolated using rabbit antibody to rat podoplanin (Sigma Chemical, St Louis, Missouri, USA) in a 1:100 dilution as the primary antibody and microbeads coupled with a secondary goat anti-rabbit antibody (MACS system, Miltenyi Biotec, Bergisch-Gladbach, Germany). The cells were grown in Dulbecco's modified Eagle medium that was supplemented with 20% fetal calf serum, 50 U/ml penicillin and 50 mg/ml streptomycin.

Measurement of contractility of lymphatic vessels

Video sequences of LVs were captured using transmitted light Axio Imager A1 microscope =with 10×0.2 Epiplan Lens (Zeiss, Germany) and monochrome CMOS camera acA1920-40um (Basler AG, Germany). Image sequences were captured with resolution of 1920×1200 pixels, 8 bit, 40 fps and stored in AVI video format. To measure lymphatic vessel diameter, the video sequence was processed with homemade software developed in LabVIEW (National Istruments Inc., USA). Walls of LVs were detected in each frame of the sequence along a line drawn across the vessel image. The IMAQ Edge Tool 3 VI (NI Vision, National Istruments Inc., USA) was used to get the position of both edges of the vessel. The resulting series of measured distances were then filtered with 4 point median filter to exclude spikes caused by detection errors related to occasional vessel movements.

Statistical analysis

The results are presented as the mean ± standard error of the mean (SEM). Differences from the initial level in the same group were evaluated by the Wilcoxon test. Intergroup differences were evaluated using the Mann-Whitney test and two-way ANOVA (post hoc analysis with Duncan's rank test). The significance level was set at $p < 0.05$ for all analyses.

Declarations

Acknowledgements

D. Li and S. Liu contributed equally to this work. This work was supported by the National Natural Science Foundation of China (NSFC) (Grant Nos. 61860206009, 81870934, 81961138015), the Science Fund for Creative Research Group of China (Grant No. 61721092), the National Key Research and Development Program of China (2017YFA0700501), China Postdoctoral Science Foundation funded project (No. BX20190131, 2019M662633); Funding for Postdoctoral Innovation Research Post in Hubei Province and the Innovation Fund of WNLO; RF Governmental Grant No. 075-15-2019-1885; Russian Science Foundation No. 20-15-00090; Russian Foundation of Basic Research No. 20-015-00308a and No. 19-515-55016 China a. The authors also thank to the Optical Bioimaging Core Facility of WNLO-HUST for support in data acquisition. DB was supported by NIH R01 NS112808.

Author contributions

D. Li was involved in the conceptualization, experiment setup, investigation, statistical analysis, writing and editing. S. Liu was involved in the conceptualization, experiment setup and investigation. Z. Liu was involved in statistical analysis. S. Sun was involved in experiment setup and investigation. T. Yu was involved in conceptualization and writing. O. Bragina performed measuring of ICP and thermal effect of PS in mice. D. Bragin was involved in measuring of ICP, writing and editing. A. Shirokov performed experiments on the LyECs. I. Fedosov was involved in measurement of contractibility of LVs. N. Navolokin collected human brain and performed ICH. J. Kurths was involved in writing and editing. O. Semyachkina-Glushkovskaya and D. Zhu were involved in writing, editing, conceptualization and project management.

Competing interests

The authors declare no competing interests.

References

1. J. An, T. J. Kim, and B. W. Yoon, "Epidemiology, Risk Factors, and Clinical Features of Intracerebral Hemorrhage: An Update," *J Stroke* **19**(1), 3-10 (2017).
2. Whitelaw A. Intraventricular haemorrhage and posthaemorrhagic hydrocephalus: pathogenesis, prevention and future interventions. *Semin Neonatol.* 2001;6:135–146.
3. Ballabh P. Intraventricular hemorrhage in premature infants: mechanism of disease. *Pediatr Res*. 2010;67(1):1-8. doi:10.1203/PDR.0b013e3181c1b176
4. Daverat, J. P. Castel, J. F. Dartigues, and J. M. Orgogozo, "Death and functional outcome after spontaneous intracerebral hemorrhage. A prospective study of 166 cases using multivariate analysis," *Stroke* **22**(1), 1-6 (1991).
5. Mohr, G. Ferguson, M. Khan et al., "Intraventricular hemorrhage from ruptured aneurysm. Retrospective analysis of 91 cases," *J Neurosurg* **58**(4), 482-487 (1983).
6. E. Hinson, D. F. Hanley, and W. C. Ziai, "Management of intraventricular hemorrhage," *Curr Neurol Neurosci Rep* **10**(2), 73-82 (2010).
7. M. Coplin, F. C. Vinas, J. M. Agris et al., "A cohort study of the safety and feasibility of intraventricular urokinase for nonaneurysmal spontaneous intraventricular hemorrhage," *Stroke* **29**(8), 1573-1579 (1998).
8. Steiner, M. N. Diringer, D. Schneider et al., "Dynamics of intraventricular hemorrhage in patients with spontaneous intracerebral hemorrhage: risk factors, clinical impact, and effect of hemostatic therapy with recombinant activated factor VII," *Neurosurgery* **59**(4), 767-773; discussion 773-764 (2006).
9. Hallevi, K. C. Albright, J. Aronowski et al., "Intraventricular hemorrhage: Anatomic relationships and clinical implications," *Neurology* **70**(11), 848-852 (2008).
10. Wilson-Costello, H. Friedman, N. Minich, A. A. Fanaroff, and M. Hack, "Improved survival rates with increased neurodevelopmental disability for extremely low birth weight infants in the 1990s," *Pediatrics* **115**(4), 997-1003 (2005).

11. J. Rooks et al., “Prevalence and evolution of intracranial hemorrhage in asymptomatic term infants,” AJNR Amer. J. Neuroradiol., vol. 29, no. 6, pp. 1082–1089, 2008
12. R. Holden, M. O. Titus, and P. Van Tassel, “Cranial magnetic resonance imaging examination of normal term neonates: A pilot study,” J Child Neurol., vol. 14, pp. 708–710, 1999
13. Vohr BR, Allan WC, Westerveld M, Schneider KC, Katz KH, Makuch RW, Ment LR. School-age outcomes of very low birth weight infants in the indomethacin intraventricular hemorrhage prevention trial. Pediatrics. 2003;111:e340–e346.
14. B. Mahaney, C. Buddhala, M. Paturu et al., "Intraventricular Hemorrhage Clearance in Human Neonatal Cerebrospinal Fluid: Associations With Hydrocephalus," *Stroke* **51**(6), 1712-1719 (2020).
15. Gao, H. Du, Y. Hua et al., "Role of red blood cell lysis and iron in hydrocephalus after intraventricular hemorrhage," *J Cereb Blood Flow Metab* **34**(6), 1070-1075 (2014).
16. S. van Solinge, I. S. Muskens, V. K. Kavouridis et al., "Fibrinolytics and Intraventricular Hemorrhage: A Systematic Review and Meta-analysis," *Neurocrit Care* **32**(1), 262-271 (2020).
17. H. Engelhard, C. O. Andrews, K. V. Slavin, and F. T. Charbel, "Current management of intraventricular hemorrhage," *Surg Neurol* **60**(1), 15-22 (2003).
18. N. Huisa, A. B. Stemer, M. G. Walker et al., "Transcranial laser therapy for acute ischemic stroke: a pooled analysis of NEST-1 and NEST-2," *Int J Stroke* **8**(5), 315-320 (2013).
19. A. Lapchak, and P. D. Boitano, "Transcranial Near-Infrared Laser Therapy for Stroke: How to Recover from Futility in the NEST-3 Clinical Trial," *Acta Neurochir Suppl* **121**, 7-12 (2016).
20. R. Hamblin, "Photobiomodulation for traumatic brain injury and stroke," *J Neurosci Res* **96**(4), 731-743 (2018).
21. Xuan, T. Agrawal, L. Huang, G. K. Gupta, and M. R. Hamblin, "Low-level laser therapy for traumatic brain injury in mice increases brain derived neurotrophic factor (BDNF) and synaptogenesis," *J Biophotonics* **8**(6), 502-511 (2015).
22. D. Morries, P. Cassano, and T. A. Henderson, "Treatments for traumatic brain injury with emphasis on transcranial near-infrared laser phototherapy," *Neuropsychiatr Dis Treat* **11**, 2159-2175 (2015).
23. R. Hamblin, "Low-Level Light Therapy," (2018).
24. Semyachkina-Glushkovskaya, A. Abdurashitov, A. Dubrovsky et al., "Photobiomodulation of lymphatic drainage and clearance: perspective strategy for augmentation of meningeal lymphatic functions," *Biomed Opt Express* **11**(2), 725-734 (2020).
25. Semyachkina-Glushkovskaya, A. Abdurashitov, M. Klimova et al., "Photostimulation of cerebral and peripheral lymphatic functions," *Translational Biophotonics* **2**(1-2), (2020).
26. Dirican, O. Andacoglu, R. Johnson et al., "The short-term effects of low-level laser therapy in the management of breast-cancer-related lymphedema," *Support Care Cancer* **19**(5), 685-690 (2011).
27. Zinchenko, N. Navolokin, A. Shirokov et al., "Pilot study of transcranial photobiomodulation of lymphatic clearance of beta-amyloid from the mouse brain: breakthrough strategies for non-pharmacologic therapy of Alzheimer's disease," *Biomed Opt Express* **10**(8), 4003-4017 (2019).

28. J. Simmonds, "The absorption of blood from the cerebrospinal fluid in animals," *Aust J Exp Biol Med Sci* **30**(3), 261-270 (1952).
29. Oehmichen, H. Gruninger, H. Wietholter, and M. Gencic, "Lymphatic efflux of intracerebrally injected cells," *Acta Neuropathol* **45**(1), 61-65 (1979).
30. M. Chen, L. M. Wang, H. Xu et al., "Meningeal lymphatics clear erythrocytes that arise from subarachnoid hemorrhage," *Nature Communications* **11**(1), (2020).
31. Sokolovski, S. G., Zolotovskaya, S. A., Goltsov, A., Pourreyron, C., South, A. P. & Rafailov, E. U. Infrared laser pulse triggers increased singlet oxygen production in tumour cells. *Rep.* **3(1)**, 3484 (2013)
32. Hoffmann, H. M & Dionne, V. E. Temperature dependence of ion permeation at the endplate channel *Gen. Physiol.* **81**, 687–703 (1983).
33. Moser, E., Mathiesen, I. & Andersen, P. Association between brain temperature and dentate field potentials in exploring and swimming rats. **259,** 1324–6 (1993).
34. Lars Kaestner, Asta Juzenienea, Johan Moana. Erythrocytes—the 'house elves' of photodynamic therapy. Photochem. Photobiol. Sci., 2004,3, 981-989
35. Ahn, J.H., Cho, H., Kim, JH. *et al.*Meningeal lymphatic vessels at the skull base drain cerebrospinal fluid. *Nature* **572,** 62–66 (2019). https://doi.org/10.1038/s41586-019-1419-5
36. I. Karu, L. V. Pyatibrat, and N. I. Afanasyeva, "Cellular effects of low power laser therapy can be mediated by nitric oxide," *Laser Surg Med* **36**(4), 307-314 (2005).
37. Shirasawa Y, Ikomi F, Ohhashi T (2000) Physiological roles of endogenous nitric oxide in lymphatic pump activity of rat mesentery in vivo. Am J Physiol Gastrointest Liver Physiol 278(4):G551–G556.
38. von der Weid PY, Zhao J, Van Helden DF (2001) Nitric oxide decreases pacemaker activity in lymphatic vessels of guinea pig mesentery. Am J Physiol Heart Circ Physiol 280(6):H2707–H2716.
39. Bohlen HG, Gasheva OY, Zawieja DC (2011) Nitric oxide formation by lymphatic bulb and valves is a major regulatory component of lymphatic pumping. Am J Physiol Heart Circ Physiol 301(5):H1897–H1906.
40. Kunert C, Baish JW, Liao S, Padera TP, Munn LL. Mechanobiological oscillators control lymph flow. Proc Natl Acad Sci U S A. 2015 Sep 1;112(35):10938-43. doi: 10.1073/pnas.1508330112
41. Gasheva OY, Zawieja DC, Gashev AA (2006) Contraction-initiated NO-dependent lymphatic relaxation: A self-regulatory mechanism in rat thoracic duct. J Physiol 575(Pt 3):821–832.
42. Louveau, I. Smirnov, T. J. Keyes et al., "Structural and functional features of central nervous system lymphatic vessels," *Nature* **523**(7560), 337-341 (2015).
43. Oehmichen, H. Wietholter, H. Gruninger, and M. Gencic, "Destruction of intracerebrally applied red blood cells in cervical lymph nodes. Experimental investigations," *Forensic Sci Int* **21**(1), 43-57 (1983).
44. E. Tedford, S. DeLapp, S. Jacques, and J. Anders, "Quantitative analysis of transcranial and intraparenchymal light penetration in human cadaver brain tissue," *Laser Surg Med* **47**(4), 312-322 (2015).

45. Wang, D. G. Ouzounov, C. Wu et al., "Three-photon imaging of mouse brain structure and function through the intact skull," *Nat Methods* **15**(10), 789-792 (2018).
46. Murad, "Discovery of some of the biological effects of nitric oxide and its role in cell signaling," *Bioscience Rep* **24**(4-5), 452-474 (2004).
47. C. Drapier, H. Hirling, J. Wietzerbin, P. Kaldy, and L. C. Kuhn, "Biosynthesis of nitric oxide activates iron regulatory factor in macrophages," *EMBO J* **12**(9), 3643-3649 (1993).
48. Lepoivre, F. Fieschi, J. Coves, L. Thelander, and M. Fontecave, "Inactivation of ribonucleotide reductase by nitric oxide," *Biochem Biophys Res Commun* **179**(1), 442-448 (1991).
49. C. Drapier, and J. B. Hibbs, Jr., "Aconitases: a class of metalloproteins highly sensitive to nitric oxide synthesis," *Methods Enzymol* **269**, 26-36 (1996).
50. Dimmeler, F. Lottspeich, and B. Brüne, "Nitric oxide causes ADP-ribosylation and inhibition of glyceraldehyde-3-phosphate dehydrogenase," *Journal of Biological Chemistry* **267**(24), 16771-16774 (1992).
51. S. Stamler, D. I. Simon, J. A. Osborne et al., "S-nitrosylation of proteins with nitric oxide: synthesis and characterization of biologically active compounds," *Proc Natl Acad Sci U S A* **89**(1), 444-448 (1992).
52. Otsu, "A threshold selection method from gray-level histograms," *IEEE transactions on systems, man, and cybernetics* **9**(1), 62-66 (1979).
53. E. Bragin, R. C. Bush, W. S. Muller, and E. M. Nemoto, "High intracranial pressure effects on cerebral cortical microvascular flow in rats," *J Neurotrauma* **28**(5), 775-785 (2011).
54. Stern-Nezer, I. Eyngorn, M. Mlynash et al., "Depression one year after hemorrhagic stroke is associated with late worsening of outcomes," *Neurorehabilitation* **41**(1), 179-187 (2017).
55. A. Francis, J. Beaumont, M. B. Maas et al., "Depressive symptom prevalence after intracerebral hemorrhage: a multi-center study," *J Patient Rep Outcomes* **2**(1), 55 (2018).
56. Zhu, Y. F. Gao, J. R. Wan et al., "Changes in motor function, cognition, and emotion-related behavior after right hemispheric intracerebral hemorrhage in various brain regions of mouse," *Brain Behav Immun* **69**, 568-581 (2018).
57. Zhu, Y. F. Gao, C. F. Chang et al., "Mouse Models of Intracerebral Hemorrhage in Ventricle, Cortex, and Hippocampus by Injections of Autologous Blood or Collagenase," *Plos One* **9**(5), (2014).
58. Bai, X. Li, M. Clay, T. Lindstrom, and P. Skolnick, "Intra- and interstrain differences in models of "behavioral despair"," *Pharmacol Biochem Be* **70**(2-3), 187-192 (2001).
59. Can, D. T. Dao, C. E. Terrillion et al., "The Tail Suspension Test," *Jove-J Vis Exp* (59), (2012).
60. Can, D. T. Dao, M. Arad et al., "The Mouse Forced Swim Test," *Jove-J Vis Exp* (59), (2012).
61. E. Renard, E. Dailly, B. A. Nic Dhonnchadha, M. Hascoet, and M. Bourin, "Is dopamine a limiting factor of the antidepressant-like effect in the mouse forced swimming test?," *Prog Neuro-Psychoph* **28**(8), 1255-1259 (2004)

Figures

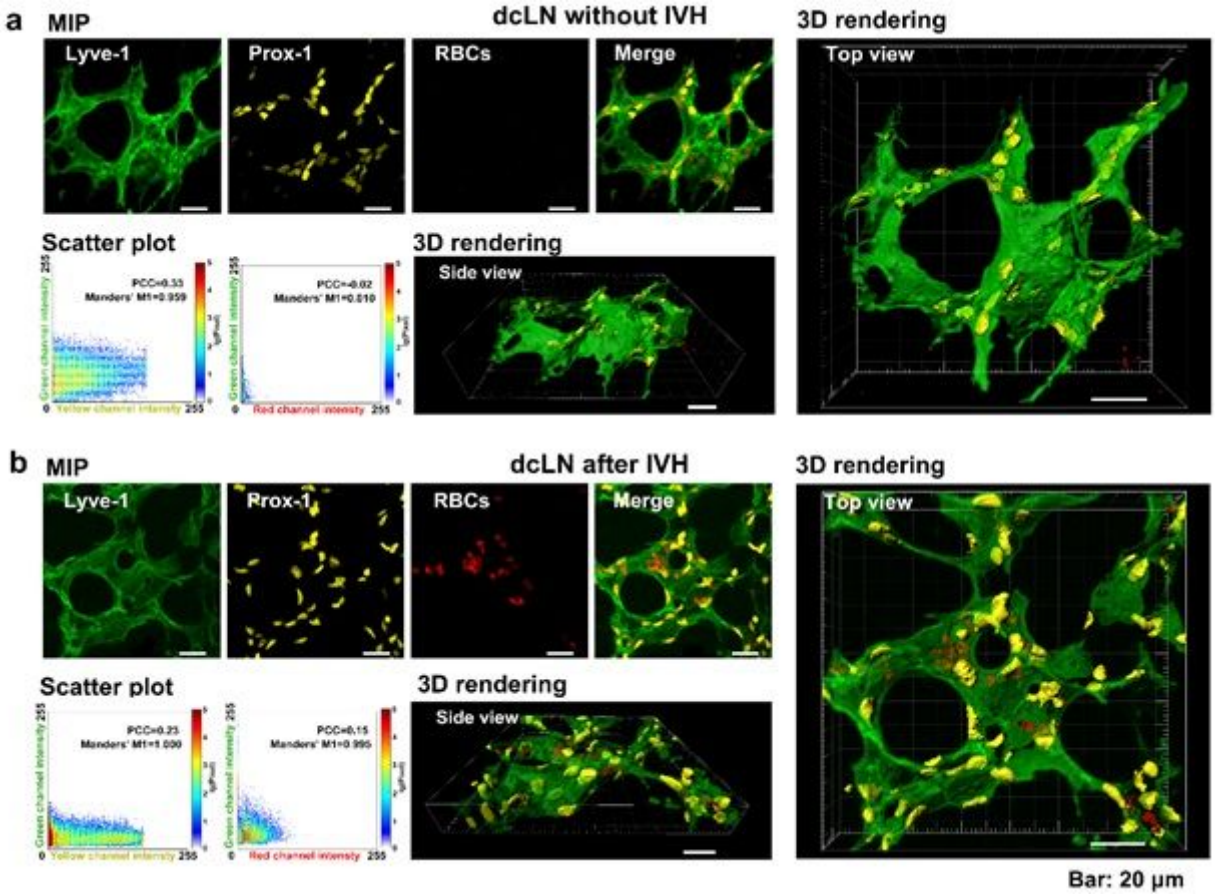

Figure 1

Clearance of RBCs from mouse brain into dcLNs: Representative images of LVs of dcLN stained for Lyve-1 (green color) and Prox-1 (yellow color) without (a) and after IVH (b). 3D rendering images illustrate the presence of RBCs inside LVs of dcLN. MIP: Maximum intensity projection. MIP: Maximum intensity projection. PCC: Pearson's correlation coefficient, which is between 1 and -1. 1 represents perfect correlation, -1 represents entirely negative correlation, and 0 represents a random relationship. Manders' M1: The proportion of the red/yellow fluorescence regions co-located with green fluorescence. Scatter plots indicate that the distribution of Prox-1 is positively correlated with Lyve-1, and almost all Prox-1 coincide with Lyve-1. In addition, the red signals which represent RBCs are negatively correlated with the distribution of Lyve-1 without IVH, suggesting there were no RBCs inside LVs of dcLNs in intact mice.

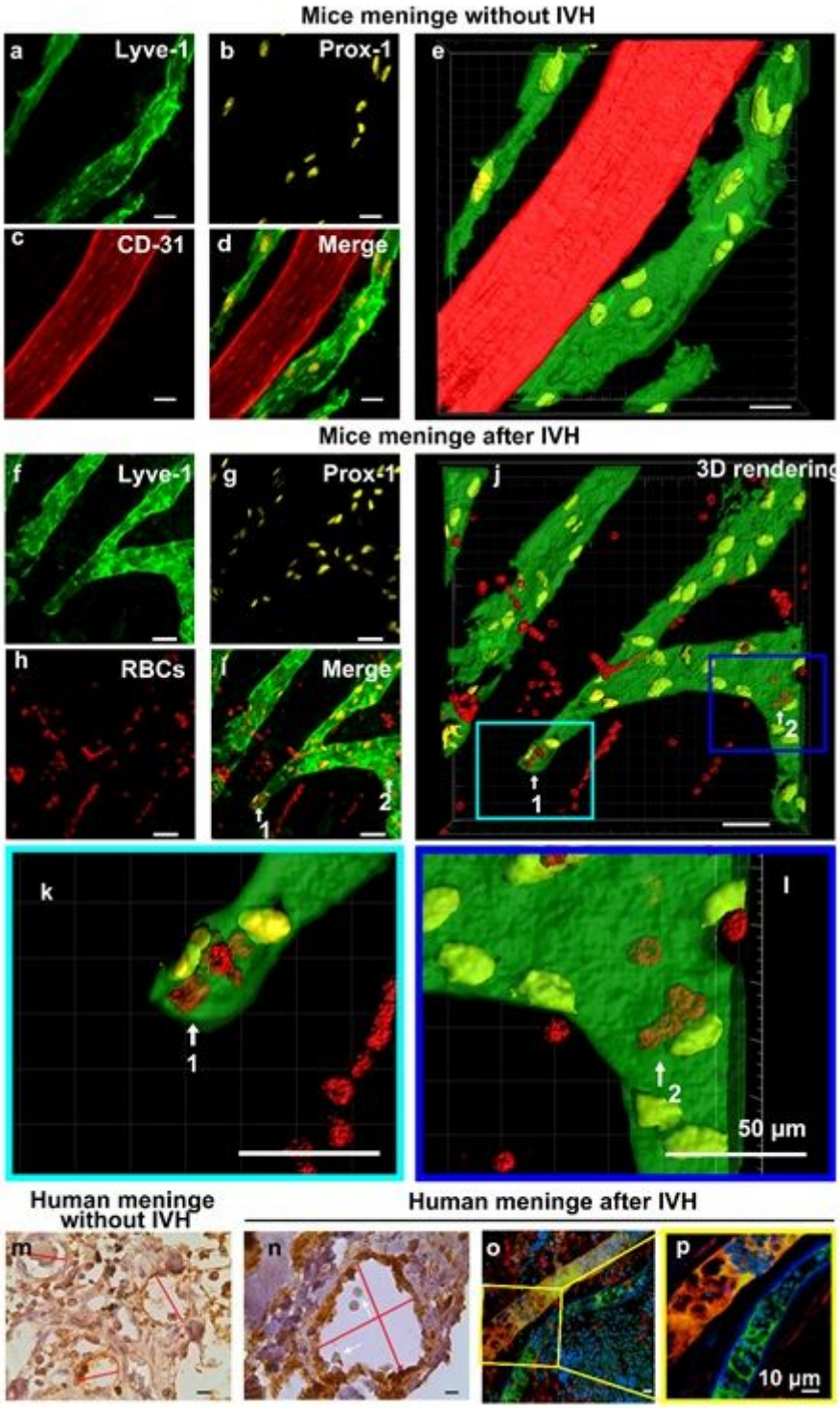

Figure 2

RBCs presence in subarachnoid space and in MLVs of mice and humans after IVH: (a-d) Representative MIP images of subarachnoid space and MLVs stained for Lyve-1 (green color) and Prox-1 (yellow color) after IVH. (a-d) Representative MIP images of subarachnoid space and MLVs stained for Lyve-1 (green color) and Prox-1 (yellow color) without IVH. (e) Multi-channel 3D rendering image. (f-i) Representative MIP images of subarachnoid space and MLVs stained for Lyve-1 (green color) and Prox-1 (yellow color) after IVH. (j) Multi-channel 3D rendering image. (k-l) Larger view of the frame areas in (e), respectively. The images clearly show that RBCs (red color) are either around MLVs or inside MLVs. Arrows 1 and 2 in

(i-l) represent RBCs inside MLVs. (m-n) Representative images of human meninges stained for Lyve-1 (brown color) without (m) and after (n) IVH. (o-p) Representative fluorescent images of the subarachnoid space and MLVs of humans stained for Lyve1 for (for the lymphatic endothelial cells), CD31 (for blood vessels), and GPA (for RBCs). Bar in (a-h): 50 μm. Bar in (i-l): 10 μm.

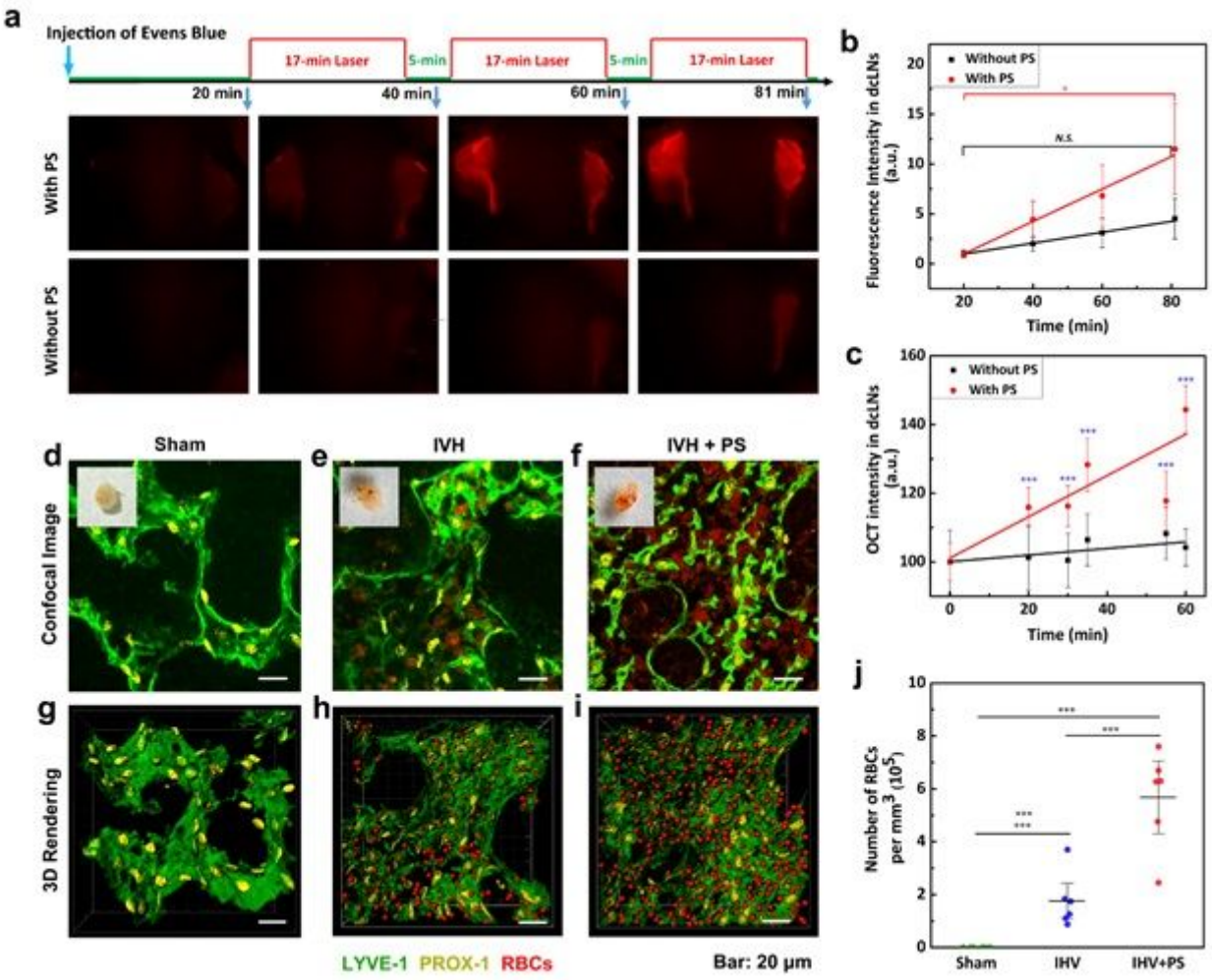

Figure 3

The PS 9 J/cm2 stimulation of lymphatic clearance of RBCs and macromolecules from mouse brain: (a) Representative fluorescent images of EBD clearance from the right ventricle into dcLNs with and without PS in intact mice; (b) Quantitative analysis of fluorescence intensity of EBD accumulation in dcLNs with and without PS; (c) the OCT data of GNRs accumulation in dcLNs after its intraventricular injection with and without PS in intact mice, * - $p<0.05$, n=10 in each group of all series of experiments; ((d-f) Confocal images of RBCs in dcLN 1 hour after the injection of saline (d), blood without PS (e) and blood+PS (f) into the right later ventricle. The insets in (d-f) represent photos of dcLN; (g) - (i) 3D rendering of distribution of RBCs in dcLN 1 hour after the injection of saline (g), blood without PS (h) and blood+PS (i) into the right later ventricle (the volume of dcLN was 135×135×40 μm3); (j) the number of RBCs in dcLN 1 hour after the blood injection into the right later ventricle with and without PS, * - $p<0.05$, *** - $p<0.001$, n=6 in each group. The LVs were labeled by Lyve-1 (green color) and Prox-1 (yellow color), RBCs were imaged with its autofluorescence (red color).

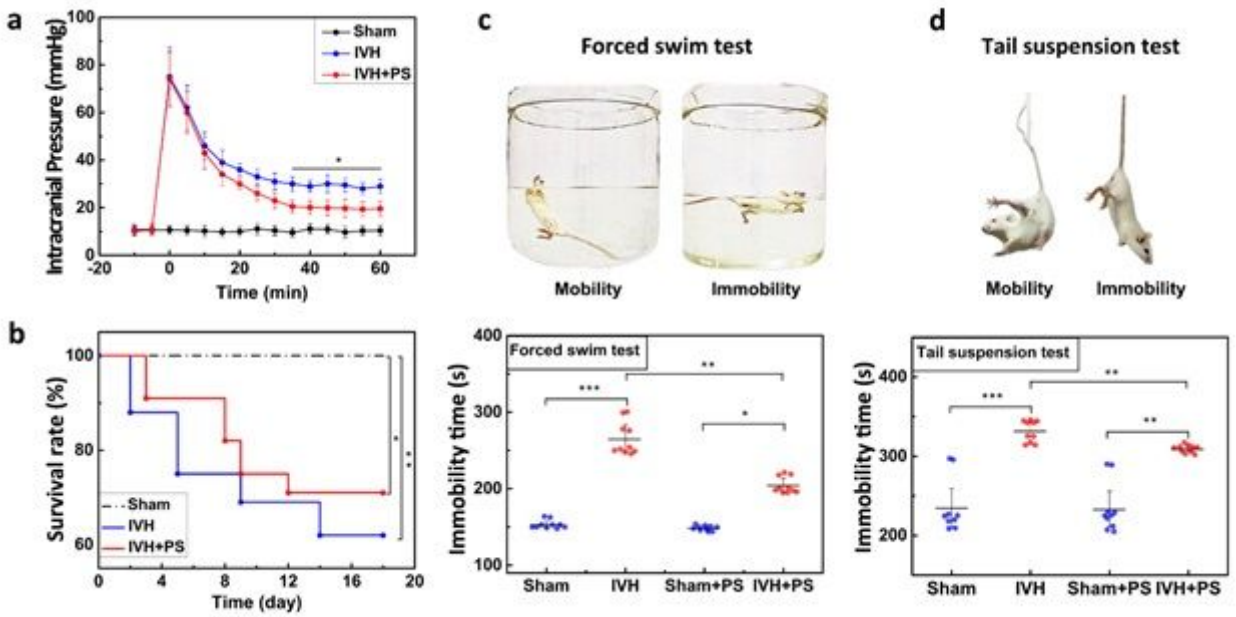

Figure 4

PS effects on ICP, the mortality rate, and emotional status: (a) – Continues monitoring of ICP after IVH with and without PS, * - p<0.05 vs. baseline level; (b) – Mortality rate in mice after IVH with and without PS; (c) and (d) Immobility time in the tail suspension (c) and in the forced swim test (d); Mean ± SD; *** - p<0.001; ** - p<0.01; * - p<0.05, n=30 per group in (b) and n=10 per group in a, c and d. All sets of experiments were performed on the sham, IVH and IVH+PS groups.

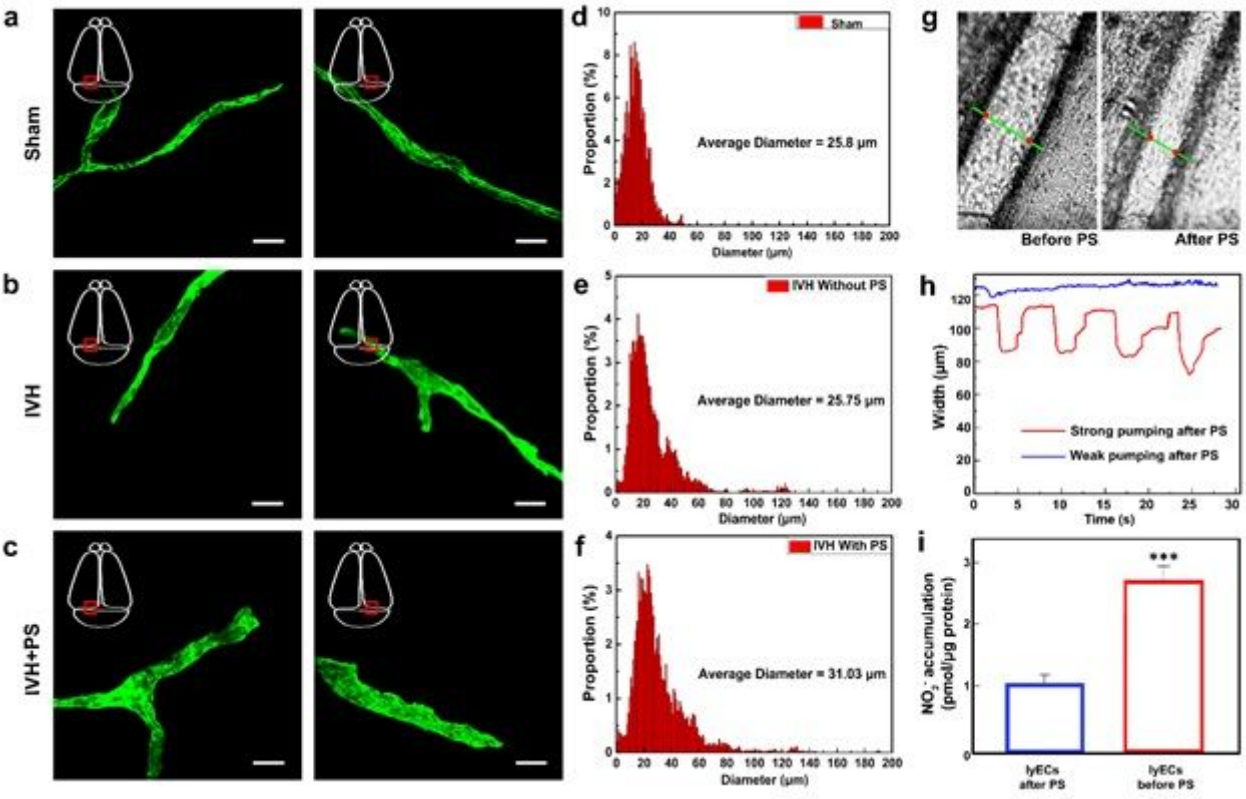

Figure 5

The mechanisms of PS effects on the LVs: (a-c) Representative fluorescent images of basal MLVs (labeled with Lyve-1) in the sham group (a), the IVH group (b) and the IHV+PS group (c). Bar: 20 μm; (d-f) Diameter of MLVs in the sham group (d), the IVH group (e) and the IHV+PS group (f). (g and h) the OCT assay of contractility of the mesenteric lymphangion, n=3, $p<0.05$. The diameter of the mesenteric lymphangion was marked in (g); (i) the production of NO (assayed as NO2-) in the medium of primary LECs, * $p<0.05$ compared with LECs without PS.

Supplementary Files

This is a list of supplementary files associated with this preprint. Click to download.

- SI20210330final.docx